In Vitro and *In Vivo* Real-Time Imaging with Ultrasonic Limited Diffraction Beams

Jian-yu Lu, *Member, IEEE*, Tai K. Song, Randall R. Kinnick, and James F. Greenleaf, *Fellow, IEEE*

Abstract—Recently, there has been great interest in a new class of solutions to the isotropic/homogeneous scalar wave equation which represents localized waves or limited diffraction beams in electromagnetics, optics, and acoustics. Applications of these solutions to ultrasonic medical imaging, tissue characterization, and nondestructive evaluation of materials have also been reported. This paper reports a real-time medical imager which uses limited diffraction Bessel beams, X waves, Axicons, or conventional beams. Results (*in vitro* and *in vivo*) show that the images obtained with limited diffraction beams have higher resolution and good contrast over larger depth of field compared to images obtained with conventional focused beams. These results suggest the potential clinical usefulness of limited diffraction beams.

I. INTRODUCTION

THE first localized solution to the isotropic-homogeneous scalar wave equation was discovered by Brittingham in 1983 [1] and was termed the "focus wave mode." This pioneer work raised research interest in localized waves. In 1985, a new localized solution to the wave equation was discovered and a method to construct other localized solutions was proposed by Ziolkowski [2]. Later, in 1989, Ziolkowski *et al.* constructed a finite energy localized wave (called a modified power spectrum pulse) and produced it with an acoustic superposition experiment [3]. The first limited diffraction beam, which is also an exact solution to the wave equation, was discovered by Durnin in 1987 and was termed a nondiffracting or diffraction-free beam [4] (we call it a "limited diffraction" beam because Durnin's original terminologies for the new beam are controversial). Durnin's beams are pencil-like and have been verified with an optical experiment [5]. Hsu *et al.* [6] have constructed the first ultrasonic limited diffraction transducer with a nonuniform poling technique and produced a CW Bessel beam. The limited diffraction beams were further studied in optics by many other investigators [7]–[12]. Lu and Greenleaf have produced Durnin's J_0 Bessel beam with a PZT ceramic/polymer composite annular array transducer and applied it to ultrasonic imaging and tissue characterization [13]–[24]. Campbell *et al.* had a similar idea to produce the J_0 Bessel beam with an annular array [25].

Based on previous studies of localized waves and limited diffraction beams by ourselves and others, we developed new families of solutions to the isotropic-homogeneous wave equation [26]–[29]. These solutions include some of the limited diffraction beams, such as Durnin's beam, in addition to an infinite number of new beams. One family of the new solutions has an X-like shape in a plane along the wave axis and we termed these "X waves" [26]. The X waves are nonspreading in both transverse and axial directions and have large depth of field even if they are produced with a finite aperture (they are different from Durnin's Bessel beams because they are nondispersive).

Large depth of field is a very desirable characteristic in imaging. A technique to increase the depth of field in medical imaging with the conventional focused beams montages the images cut from various focal depths to form a frame of an image, with an accompanying decrease in the imaging frame rate. With the limited diffraction beams, the montaging process may not be needed because of their large depth of field. Therefore, high-resolution images with a high-frame rate may be obtained with the limited diffraction beams.

In this paper we compare real-time medical ultrasonic images produced using several types of incident ultrasonic beams: an X wave, a J_0 Bessel beam, conventional focused beams, and an Axicon beam. For a given imaging trial, a single multi-element transducer was used, operated in pulse-echo mode and scanned using a commercial "wobbler" mechanism. In all cases the electrical signals generated by the returning ultrasound echoes were processed in the same manner using a classic dynamic-focusing process. The imaging resolution, contrast, and depth of field of the limited diffraction beams will be evaluated *in vitro* and *in vivo*.

The paper is organized in the following way. In Section II we present a theoretical description of n-dimensional limited diffraction beams, especially, the X waves. The system we used for producing both the limited diffraction beams and the conventional focused beams is described in Section III. The *in vitro* and *in vivo* real-time imaging experiments and their results are reported in Sections IV and V, respectively, and discussion and conclusions are given in Sections VI and VII, respectively.

II. THEORETICAL PRELIMINARIES: DIFFRACTION LIMITED SOLUTIONS TO THE SCALAR WAVE EQUATION

Propagation of acoustic, electromagnetic, and optical waves is governed by wave equations. An n-dimensional isotropic-

homogeneous scalar wave equation is given by [30]

$$\left[\sum_{j=1}^{n} \frac{\partial^2}{\partial x_j^2} - \frac{1}{c^2} \frac{\partial^2}{\partial t^2} \right] \Phi = 0 \qquad (1)$$

where x_j, $(j = 1, 2, \cdots, n)$, are n rectangular spatial coordinates, n is an integer, t is time, c is a constant, and $\Phi = \Phi(x_1, x_2, \cdots, x_n; t)$ represents an n-dimensional wave field.

It is easy to prove that the following function is one of the special solutions of the wave equation [16]:

$$\Phi(x_1, x_2, \cdots, x_n; t) = f(s) \qquad (2)$$

where

$$s = \sum_{j=1}^{n-1} D_j x_j + D_n(x_n - c_1 t), \quad (n \geq 1) \qquad (3)$$

and where

$$c_1 = \pm c \sqrt{1 + \sum_{j=1}^{n-1} D_j^2 / D_n^2}, \quad (n \geq 1) \qquad (4)$$

and where D_j are any complex coefficients which are independent of the spatial and time variables, $f(s)$ is any complex function (well-behaved) of s, and $n \neq 0$ (if $n = 0$, $f(s)$ is only a function of time and does not represent a wave).

Equation (2) represents limited diffraction beams if c_1 in (4) is real [16]. We use the term *limited diffraction* to mean that if one travels with the waves at the phase velocity, c_1, in an n-dimensional space along the axis, x_n, the wave patterns are unchanged with time.

Examples of the limited diffraction beams for different n are given by [16]. One specific example is the X wave [26]. The X wave is constructed by letting $n = 3, x_1 = x,\ x_2 = y,\ x_3 = z,\ D_1 = \alpha_0(k, \zeta) \cos \theta,\ D_2 = -\alpha_0(k, \zeta) \sin \theta$, and $D_3 = b(k, \zeta)$, where θ, k and ζ are free parameters which are independent of the spatial variables, $\vec{r} = (x, y, z)$, and time, t, and $\alpha_0(k, \zeta)$ and $b(k, \zeta)$ are any complex functions (well-behaved) of k and ζ. Equation (4) is rewritten (taking the "+" sign, thus considering only the forward propagating waves) as

$$c_1 = c \sqrt{1 + \alpha_0^2(k, \zeta) / b^2(k, \zeta)}. \qquad (5)$$

The solutions $f(s)$ for any k and θ can be summed and remain solutions to (1). Therefore we integrate $f(s)$ over the free parameters k and θ, constructing a family of solutions [26]

$$\Phi_\zeta(s) = \int_0^\infty T(k) \left[\frac{1}{2\pi} \int_{-\pi}^{\pi} A(\theta) f(s) d\theta \right] dk \qquad (6)$$

where $T(k)$ is any complex function (well-behaved) of k, and $A(\theta)$ represents any complex weighting function (well-behaved) of the integration with respect to θ. If c_1 in (5) is independent of k, the summation of $f(s)$ over k preserves the phase velocity, and thus still represents a limited diffraction beam.

We can find practical solutions by incorporating a system transfer function, $B(k)$, and represent both broad band and

band-limited X wave solutions. A zero-order X wave [26] is obtained from (6) if $\alpha_0(k, \zeta) = -ik \sin \zeta$, $b(k, \zeta) = ik \cos \zeta$, $f(s) = e^s$, $A(\theta) = 1$, and $T(k) = B(k)e^{-a_0 k}$ (note that from (5), $c_1 = c/\cos \zeta$, which is independent of k). The resulting solution is [26],

$$\Phi_{XBL_0} = \frac{1}{a_0} \mathcal{F}^{-1} \left[B\left(\frac{\omega}{c} \right) \right] * \Phi_{XBB_0} \qquad (7)$$

where

$$\Phi_{XBB_0} = \frac{a_0}{\sqrt{(r \sin \zeta)^2 + [a_0 - i(z \cos \zeta - ct)]^2}} \qquad (8)$$

and where $B(k)$ is any well-behaved complex function of $k = \omega/c$ (it can represent the transfer function of any practical linear system), ω is an angular frequency, $r = \sqrt{x^2 + y^2}$, and $a_0 > 0$ is a constant. The subscripts "BL" and "BB" represent band-limited and broadband, respectively.

In the next section, we will describe the design of an ultrasonic annular-array transducer which can be driven to produce either limited diffraction beams or conventional focused beams.

III. SYSTEM DESIGN AND BEAM CALIBRATION

A. Transducer Design

A 14-element annular array transducer was designed to produce the limited diffraction beams and the conventional focused beams. The transducer has a diameter of 25 mm and a central frequency of 3.5 MHz. The curvature of the transducer is 85 mm which gives a natural focal length of about 85 mm. The -6 dB pulse-echo (two-way) bandwidth of the transducer is about 50% of the central frequency. The transducer is made of PZT ceramic/polymer composite material and is sandwiched between a front matching layer and a low-impedance absorbing backing layer. The transducer elements were formed by first dividing the electrode on the back side of the active material (the electrode on the front side was grounded) into five rings according to the five lobes of the Bessel function, $J_0(\alpha r)$, where $\alpha = 1.21751$ mm^{-1} is a scaling factor, $r \leq 12.5$ mm is the radial distance from the center of the transducer, and J_0 is the zero-order Bessel function of the first kind. Then, the central ring was subdivided into 2 rings of equal width. The second to the fifth rings were each subdivided into 3 rings of equal width to form a total of 14 elements (rings). With the above scaling factor, α, the -6-dB beam width of the Bessel beam is about 1.98 mm, and this can be taken as a criterion of the lateral resolution of the J_0 Bessel beam. The outer radii of the 14 elements are 0.888, 1.876, 2.729, 3.582, 4.435, 5.293, 6.151, 7.009, 7.868, 8.727, 9.586, 10.447, 11.309, and 12.5 mm, respectively (the gaps between the elements were about 0.2 mm). The transducer was mounted in a commercial mechanical scan head (wobbler) and wired and cabled by Echo Ultrasound[1] (Fig. 1) to perform real-time sector scans.

It should be noted that after the transducer was constructed, the 14th element of the transducer was found to be inoperative
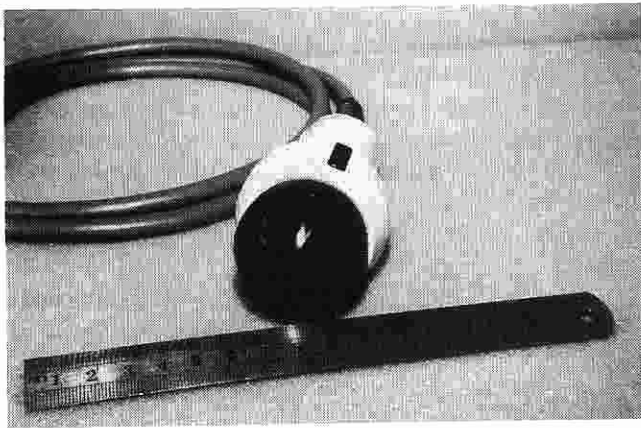
Fig. 1. A 14-element, 3.5-MHz central frequency, and 25-mm-diameter annular array transducer (wobbler) which is scanned mechanically and is capable of producing X wave, Bessel beam, and conventional focused beams, etc.
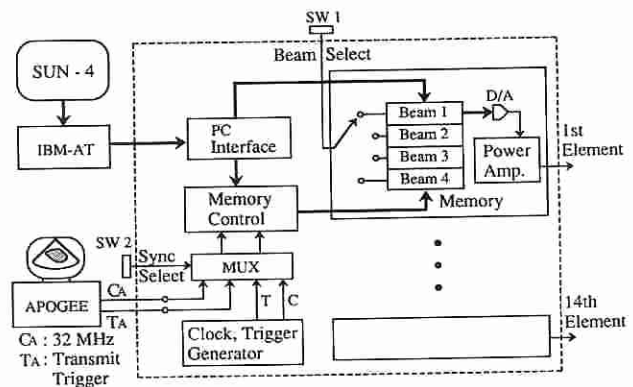

Fig. 2. Block diagram of a digital waveform synthesizer. It has 14 channels and can generate 14 excitation waveforms simultaneously. Digital excitation waveforms produced in a SUN SPARCstation 2 workstation were loaded to the memories of the digital waveform synthesizer and read out via D/A converters with either internal or external clocks (30 MHz for internal clock and 32 MHz for clock from the APOGEE CX scanner). The analog signals were amplified by power amplifiers to excite the transducer elements. The memories (8 kilobytes for each channel) were designed to hold as many as 4 sets of excitation waveforms for 4 different beams. The specific beam is selected with a switch on the front panel.

(sensitivity is almost zero). This reduces the actual diameter of the transducer to about 22.6 mm, shortening the depth of field of the limited diffraction beams. When the transducer is used in a receiving mode, its 14 elements are grouped into 6 annuli of approximately equal area: I=1+2+3+4+5+6, II=7+8, III=9+10, IV=11+12, V=13, and VI=14, where I, II, III, IV, V, and VI represent combined elements, and 1, 2, 3, ···, 14 are original elements. Since the 14th element is dead, only five elements or channels are actually used in receive.

B. Digital Waveform Synthesizer

A flexible system for testing various beams in real-time imaging was designed and constructed using a digital waveform synthesizer for each of the 14 transducer elements (see Fig. 2). Digital excitation waveforms (8 bits) were synthesized in a SUN SPARCstation 2 workstation and transferred to the digital waveform synthesizer via the Ethernet™ network and an IBM-AT personal computer (PC). The IBM-AT was interfaced to the digital waveform synthesizer with a PC interface as shown in Fig. 2. The waveform synthesizer was driven from either internal (30 MHz) or external (such as from an APOGEE CX scanner (32 MHz)) sync sources which were chosen by a switch (SW2).

The signal storage memory for each channel had a capacity of 8 kilobytes. Each memory was divided into 4 segments of 2 kilobytes available for each transmit waveform (which were about 64 μs long at a clock rate of 32 MHz). The 4 segments of the memory in each channel were used to store 4 excitation waveforms from 4 different beams. The excitation waveforms were converted to analog waveforms by 14 eight-bit D/A converters capable of outputting bipolar signals. These analog waveforms were amplified by power amplifiers to excite the transducer elements. Each of the 4 different beams stored in the memories can be chosen by a switch (SW1) on the front panel.

C. Beam Calibrations

To produce different beams, aperture weighting (apodization) must be applied. Because there are only a finite number of elements, a continuous aperture voltage weighting is not possible and a stepwise approximation must be used. If the sensitivities of all of the transmitting channels are the same, a stepwise weighting function for producing the X wave can be calculated from (8) by setting $z = 0$ mm and $r = r_q$, $(q = 1, 2, \cdots, 14)$, where r_q are the central radii of the elements (i.e., $r_q = 0.000, 1.4820, 2.4025, 3.2555, 4.1085, 4.9640, 5.8220, 6.6800, 7.5385, 8.3975, 9.2565, 10.1165, 10.9780, 12.0045$ mm, respectively). This weighting function is time dependent and is similar to that shown in Fig. 3 of [27]. Since the geometry of the transducer elements was designed from a J_0 Bessel function, the transducer is handy for producing the J_0 Bessel beam. Similar procedures can be followed to produce stepwise Bessel weighting by substituting $r = r_q$, $(q = 1, 2, \cdots, 14)$, into the function, $J_0(\alpha r)$, or to produce stepwise weightings for the conventional focused beams such as the Gaussian beam.

In practice, the sensitivities of the transmitting channels (transducer element along with its associated power amplifier) are different because of various factors such as the different capacitance of each element and the nonlinearity of the power amplifiers working at high voltages. Therefore, sensitivity calibration for each channel is necessary. Because the power amplifiers were slightly nonlinear, calibration was done for each beam. To calibrate, the excitation signals were generated and theoretical aperture weightings were applied. For the X wave, the excitation signals and aperture weighting were calculated simultaneously from (8), while for the Bessel beam and the conventional focused beams, the excitation signals were one-and-a-half-cycle short pulses (3.5-MHz central frequency) weighted in the aperture according to the type of beam to be produced. The excitation signals were first generated and stored as data files in the SUN SPARCstation 2 computer with a sampling rate of 32 megasamples/second (the excitation signals were filtered and their highest frequency component was limited to 10 MHz to avoid aliasing [31]), then the data
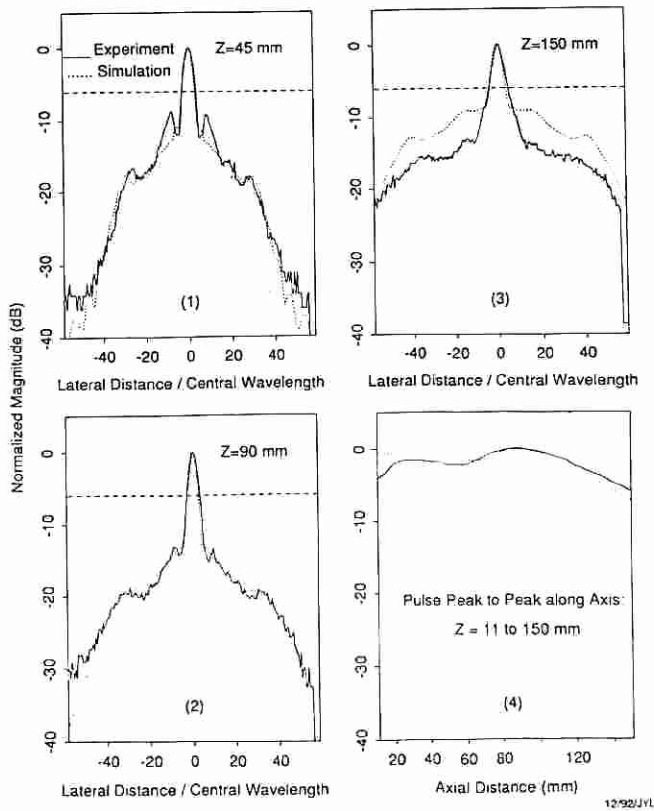
Fig. 3. Lateral and axial line plots of the X wave produced by the 14-element transducer in Fig. 1. Full lines and dotted lines represent experiment and simulation results, respectively. Dashed lines indicate the −6-dB level of the beams from their maxima. Panels (1), (2), and (3) show the lateral line plots in which the maximum magnitude of each A-line is plotted over the lateral direction to show the maximum sidelobes of the X wave at axial distances, $z = 45$, 90, and 150 mm, respectively. The lateral axes of the plots represent the lateral distance divided by the central wavelength of the transducer (0.429 mm) and the vertical axes represent the magnitudes of the pulses normalized to their maxima. Panel (4) shows the peak-to-peak values of the X wave pulses along the axis of the transducer from distance, $z = 11$ to 150 mm (z starts from the surface of the active transducer elements).

were transferred to the memories of the digital waveform synthesizer in the transmitter, converted to analog signals, and amplified to drive the transducer elements. To adjust the acoustic output of each channel, the peak-to-peak pressures of pulses were calculated (assuming equal sensitivity for all channels) for an axial distance 100 mm from the surface of the transducer for each beam using the Rayleigh-Sommerfeld formulation of diffraction [32]. The axial distance of 100 mm was chosen to avoid rapid variation of the pressure fields from the outer elements of the transducer while at the same time keeping the influence of water nonlinearity as small as possible. Then, the transducer was excited element by element by the appropriate waveform, and the pressure fields on axis at 100 mm were measured in water with a 1-mm-diameter calibrated broadband hydrophone (Medicoteknisk Institut) and an oscilloscope (Tektronix 2445B, 150 MHz). The aperture weighting of each channel was corrected by multiplying the excitation signal of that channel with the ratio between the simulated and measured values in the computer (SUN SPARC-station 2). This procedure was executed for several iterations because of the nonlinearity of the power amplifiers. In addition to the sensitivity compensation, the curvature of the transducer

and its spherical cap were compensated by changing the delays of the excitation signals in the computer to match the measured pulse with the calculated pulse. Because the system works in a pulse-echo mode, the time duration of each excitation signal can not be too long. In our experiment, the length of all excitation signals was set to 14 μs (448 points when the sampling rate is 32 mega-samples/second). After the calibrations, all of the transducer elements were excited simultaneously to produce the complete beams.

Lateral and axial beam measurements of the calibrated X wave in water were compared to their simulation (Fig. 3). The lateral line plots were obtained by measuring the maximum magnitude of each A-line and plotting it over the lateral direction to show the maximum sidelobes of the X wave. The following parameters of the X wave were used in both the experiment and the simulation: $a_0 = 0.05$ mm, and $\zeta = 4.75°$. The depth of field of the X wave calculated by the formula [26], $Z_{max} = a \cot \zeta$, where a is the radius of the transducer, is about 150.4 mm. The difference between the experiment and simulation may result from the influence of the nonlinearity of water and the compensation error of the curvature of the transducer. Since the 14th element of the transducer is broken, the depth of field of the X wave is reduced to about 136.1 mm (radius is reduced from 12.5 to about 11.3 mm). For the Bessel beam, the depth of field is determined by Durnin's formula [4], [5]. With the parameters, $\alpha = 1.21751$ mm^{-1} and the central frequency of 3.5 MHz, the depth of field of the J_0 Bessel beam in water is about 150 mm, which is reduced to about 135.7 mm without the 14th element. Line plots (similar to Fig. 3) for the Bessel beam and the conventional focused beams measured in water agreed well with their simulation results (not shown).

IV. IMAGING EXPERIMENT

An APOGEE CX B-scanner was modified by Interspec[2] to interface with the 14-channel transmitter made in our laboratory. The modified scanner allows our 14–element transducer to transmit and combines 14 received echo signals to 6 of approximately equal areas of the combined elements of the transducer, and processes the signals using the original 6-channel dynamic-focusing receiver of the APOGEE CX. Because the excitation signals may not be zero for $t < 0$ (8), the center of the excitation waveforms (7 μs, total was 14 μs) was chosen as $t = 0$. To synchronize the transmitting and receiving start time, a modified transmit trigger which is 7 μs ahead of the APOGEE regular transmit trigger was used for the 14-channel synthesizer. The position sensor inside the probe synchronized the mechanical sector scans to the APOGEE CX system to form images. Figure 4 shows a photograph of the modified APOGEE CX system and the 14-channel transmitter as well as the water tank where an ATS539 phantom was being scanned. The video images from the APOGEE CX were digitized at 7 bits by a SUN VideoPix SBus card via a 75Ω cable and rescaled to 8 bits to be printed out.

For the *in vitro* experiments, the objects to be scanned were immersed in the water tank (as shown in Fig. 4) and the probes were held firmly with clamps. The water was degassed
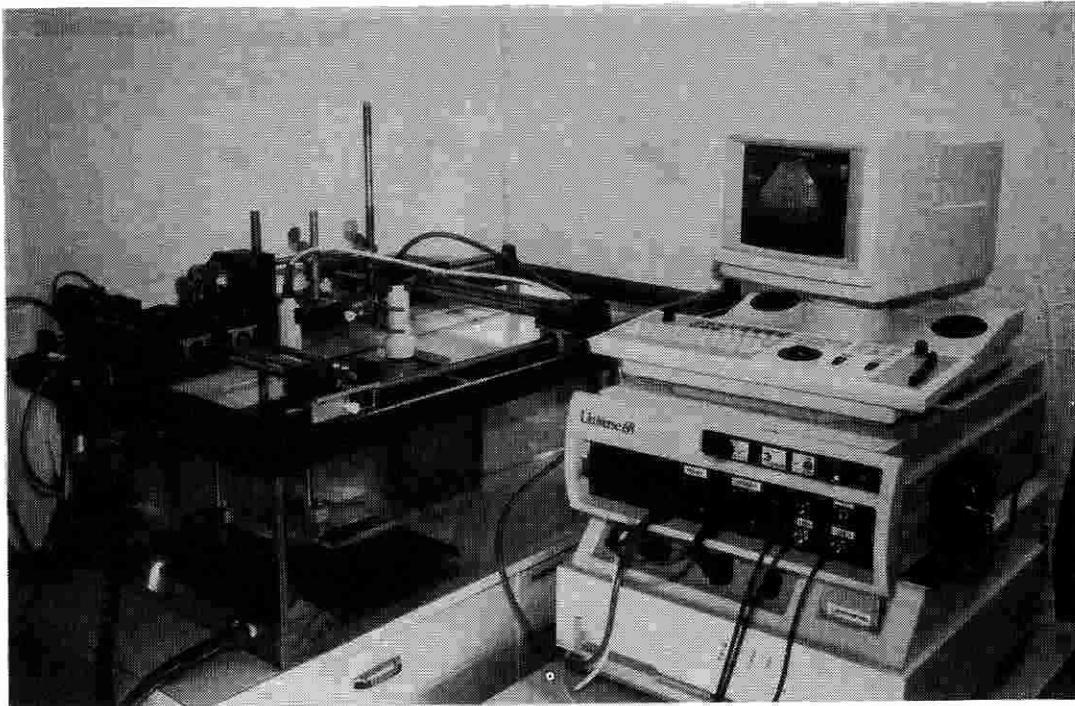
Fig. 4. The modified APOGEE CX scanner and the 14-channel transmitter made in our laboratory. On the left-hand side of the scanner, there is a water tank with a multiple axis scanner. An ATS539 multipurpose phantom was laid on a plexiglass platform and scanned with the 14-element probe which was clamped firmly above the phantom. A cross section of the phantom was displayed on the APOGEE CX monitor. The video image was digitized and stored to a SUN SPARCstation 2 workstation via a standard video output of the APOGEE CX.

and heated to about 37°C. The objects could be moved in 3 perpendicular directions. For the *in vivo* experiments, a sonographer and a cardiologist scanned volunteers. In these experiments, the preprocessing, postprocessing, and gamma processing parameters of the APOGEE CX were held constant. The TGC (time-gain control) slides were adjusted so that the images were the "best" to the observers. The scale for distance in the images is relative to the cap surface of the probes (the distance between the center of the transducer elements to the surface of the cap is about 8 mm). Other imaging parameters, such as, image frame rate, angle of view, penetration depth, and central frequency, etc., are indicated in the images.

In the next section, we describe and illustrate frozen frames of real-time images of a phantom and human organs (*in vitro* and *in vivo*) obtained with the above imaging system which transmits using several types of beams and receives echoes with the APOGEE CX dynamically focused receiving system.

V. RESULTS

A. In Vitro

A commercial ATS539 multipurpose phantom was used in the experiment. The phantom is composed of a scattering tissue-mimicking material. It is rubber based (Urethane rubber) and, at 23°C, has an attenuation coefficient of about 0.5 dB/cm/MHz and a speed of sound of about 1.45 mm/μs. The phantom contains thin wires (monofilament nylon of about 0.12 mm diameter), echo-free cylinders (diameters: 8, 6, 4, 3, 2 mm, respectively), and cylinders of different contrasts (15

dB to -15 dB with diameter of 15 mm) for testing imaging resolutions and contrasts. The dimension of the phantom is 197 mm (width) $\times$ 165 mm (height) $\times$ 80 mm (thickness).

Figure 5 shows images of a cross section of the ATS539 multipurpose phantom with an X wave, a J_0 Bessel beam, a focused unweighted beam, and a focused Gaussian beam. From left to right of each panel in Fig. 5 we see the images of the thin wires, the echo-free cylinders of different sizes, and the cylinders of different contrasts. These images represent exactly the same cross section of the phantom since the relative position of the probe and the phantom was fixed (the only change was to transmit different beams with different excitation signals).

To compare the different beams on imaging objects that present some degree of phase aberration (variation of speed of sound), a human liver sample (Fig. 6) was prepared. The liver sample came from an autopsy and was degassed and fixed in a 10% formalin fluid. The liver sample was placed in a plexiglass box and the top of the box was sealed with a polyester film of thickness of 0.125 mm to act as an acoustic window [14]. The liver sample inside the box was oriented in such a direction that the scan through the acoustic window provides images normally obtainable from clinical imaging (Fig. 7).

B. In Vivo

A middle-aged volunteer was scanned to image his liver. The volunteer sat on a chair and held his breath during the scan. Approximately the same cross sections of the liver were scanned (see Fig. 8).
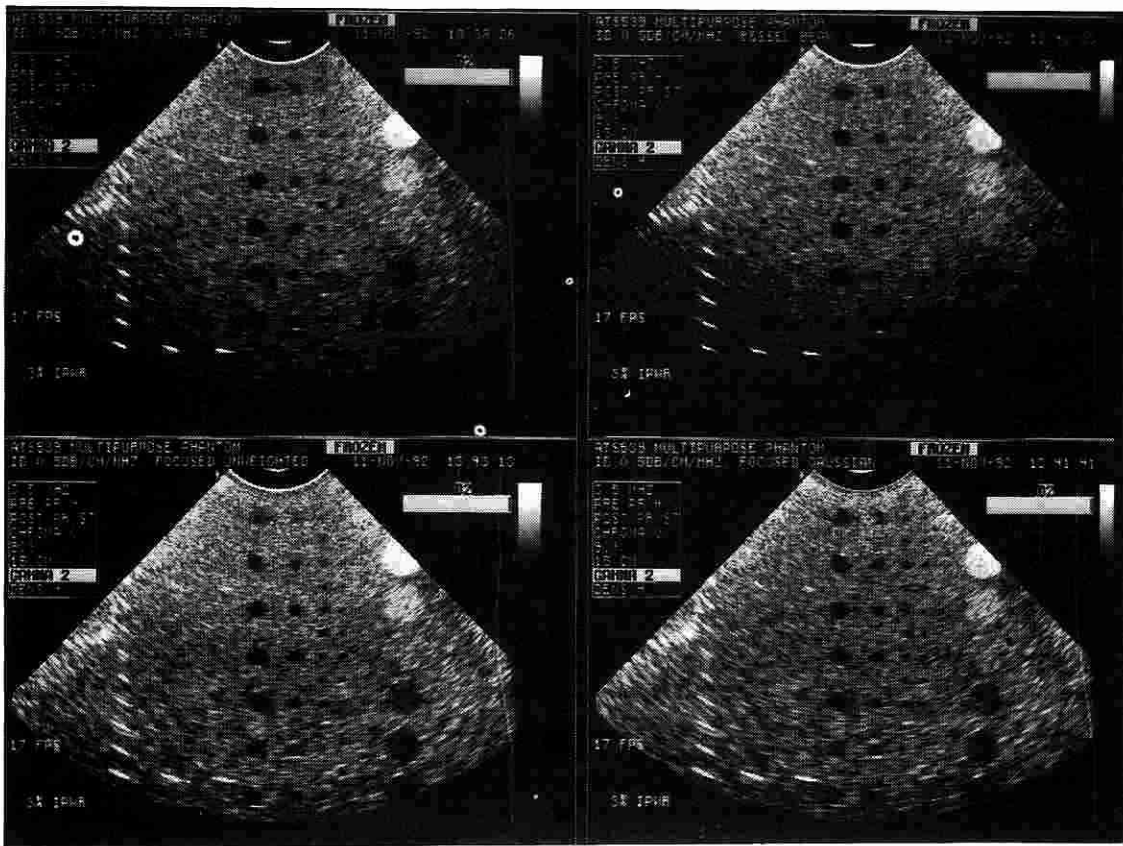
Fig. 5. Images of a cross section of the ATS539 multipurpose phantom. The images (from left to right and from top to bottom) were obtained by transmitting with X wave, Bessel beam, focused unweighted beam, and focused Gaussian beam (12.5-mm full width at half maximum (FWHM) of the aperture voltage weighting), respectively, with our 14-channel transmitter and the 14-element transducer. Echo signal processing was with the APOGEE CX 6-channel dynamic-focusing receiver (in which the 14 transducer elements were combined into 6 groups of about equal areas). For the conventional focused beams, the focal length was 85 mm (78 mm from the cap of the probe). The transmitting focal lengths of the conventional beams are indicated with the "$\bigcirc$" sign (X wave and Bessel beam are focused throughout the region). The depths of the images were set to 15 cm (from the cap of the probe) in the APOGEE CX scanner. The imaging frame rate, preprocessing, postprocessing, and angle of view are shown in the images. TGC (time-gain control) curves were adjusted for individual image so that the image displays had similar brightness. The displayed transmitting powers are invalid since our transmitter was used.

In heart imaging, another middle-aged volunteer was scanned. The volunteer laid on a bed on his left side with his left arm raised. A cardiologist scanned a long axis view of the heart and tried his best to locate the same cross sections of the heart with the different beams. The last 32 frames of images of the scan can be stored in the digital memory of the APOGEE CX as a cine loop and can be played back after the system enters a frozen mode. Images that represented about the same moments in a cardiac cycle were chosen from each cine loop and digitized. The digitized images are shown in Fig. 9.

VI. DISCUSSION

A. Resolutions

Images obtained with the limited diffraction beams (X wave and Bessel beam) have higher lateral resolution over a large depth of field as compared to those obtained with the conventional focused beams (Fig. 5, Figs. 7 to 9). The axial resolution of the images is about the same for all of the beams

and depends mainly on the bandwidth of the transducer. The nylon wires, which appear as small, white ovals in the left half of each panel in Fig. 5, show clearly both the lateral and the axial resolutions of each beam. Images with the limited diffraction beams present uniformly high lateral resolution of the wire pattern over the expected depth of field.

B. Contrast

The contrast of the images obtained with the limited diffraction beams is good. All the echo-free holes and cylinders with different contrasts which are resolvable by the conventional focused beams are resolvable by the limited diffraction beams (Fig. 5). The regions at deeper depths of the images obtained with the limited diffraction beams appear to be darker. This is because the overall power of the limited diffraction beams is insufficient (the maximum voltage range of our prototype transmitter is around $\pm$ 80V, and the aperture weightings of the transducer drop the voltages applied to the outer elements). The lack of power in the deeper depths requires the TGC to be set to higher values, which uncovers noise from the digital
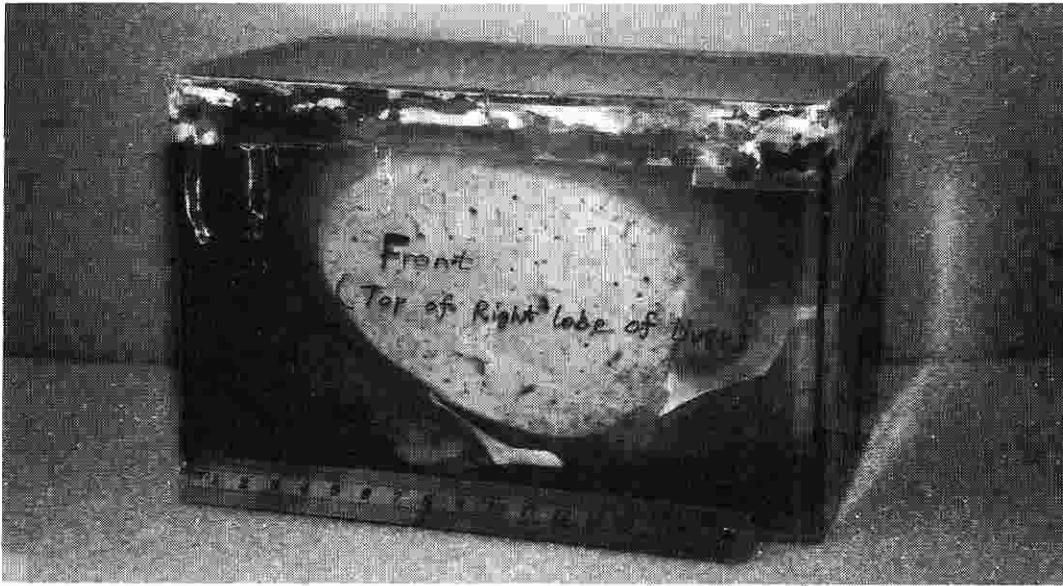
Fig. 6.   An excised human liver sample. The plexiglass box is 207 mm (width) × 131 mm (height) × 118 mm (thickness).
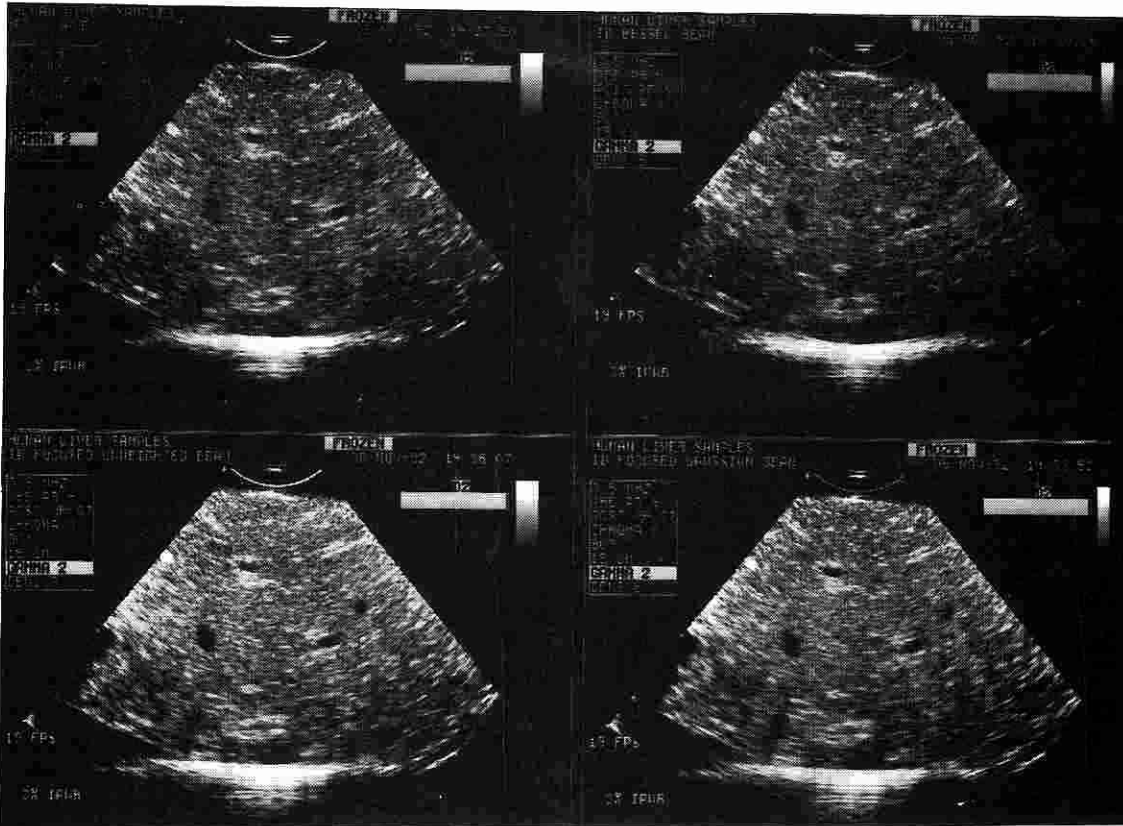

Fig. 7.   Images of a cross section of the human liver sample in Fig. 6. The images have the same format as that of Fig. 5 and the procedures used to obtain the images are the same.

board of our 14-channel transmitter and reduces the image contrast to some degree. For the conventional focused beams, the situation is a little better because the focusing increases the beam intensity around the focal regions. The power level of the 14-channel transmitter appears to be around 2–3% of the full power of the APOGEE CX when used with its original 3.5-MHz, 19-mm-diameter, 6-element probe.

C. Depth of Field

Deep depth of field is obtained in current clinical scanners by transmitting at several focal depths and montaging the images together. This reduces the imaging frame rate leading to blurred images of moving organs such as the heart. The depth of field of the limited diffraction beams is
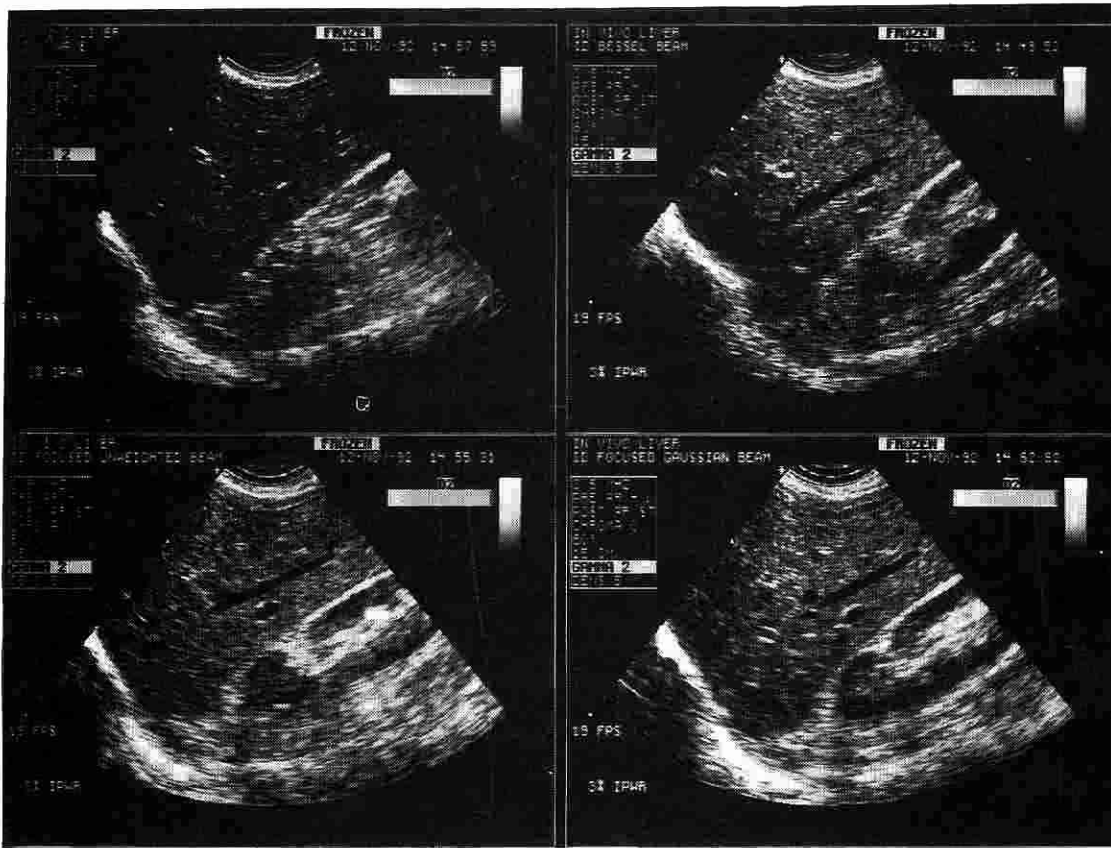
Fig. 8. *In vivo* images of a human liver. The images have the same format as that of Fig. 5. The procedures for obtaining the images are about the same as those in Fig. 5.

large compared to those of the conventional focused beams (focal length is about 85 mm) at the same imaging frame rate (Fig. 5, Figs. 7 to 9). The calculated depth of field of the limited diffraction beams is about 150 mm. Since the 14th element of the transducer was broken during the manufacturing, the effective diameter of the transducer was reduced to about 22.6 mm and this gives a depth of field of about 135 mm.

D. Phase Aberration

The images obtained with both the limited diffraction beams and the conventional focused beams (see Figs. 7 to 9) show no noticeable influence of phase aberration caused by the tissue inhomogeneities. In other words, tissue inhomogeneities would have similar influence on both the limited diffraction beams and the conventional focused beams. Since the limited diffraction beams involve aperture weightings, the influence of the phase aberration of the tissues could be less than that of unweighted beams such as a piston drive.

E. Imaging with Other Limited Diffraction Beams

In addition to the limited diffraction beams studied above (X wave and Bessel beam), other limited diffraction beams that are given by (6) can also be studied on the real-time imaging system with the 14-element transducer. For example, by choosing $f(s)$ other than e^s or choosing other $A(\theta)$,

entire new families of beams can be studied (their sidelobes, frequency spectra, and the total energy might be different from those of the X waves). Although analytic solutions may not be obtained for the other limited diffraction beams, the excitation signals of the transducer may be numerically calculated and produced with the 14-channel transmitter. Localized waves such as the focus wave mode and modified power spectrum pulses [1]–[3] can also be studied.

F. X Wave Pulse-Echo Imaging System

The X wave is non-spreading in both lateral and axial (nondispersive) directions within its depth of field. Therefore, it is possible to deconvolve pulse-echo images with only one kernel if the X wave is used in both transmitting and receiving because the point spread function of the X wave imaging system is linear and shift-invariant in space. This will produce a high resolution and low sidelobe image if the objects to be imaged do not have severe phase aberration and strong multiple reflections [33]. Deconvolution (2-D Wiener filtering) of a pulse-echo image of an RMI413A tissue-equivalent phantom with only one deconvolution kernel has been reported [16], [23], where the image was obtained experimentally with a broadband J_0 Bessel beam in both transmitting and receiving. Although the broadband Bessel beam is only nonspreading in the lateral direction within its depth of field, the results have already shown increased resolution and reduction of sidelobes (see Fig. 12 of [16]).
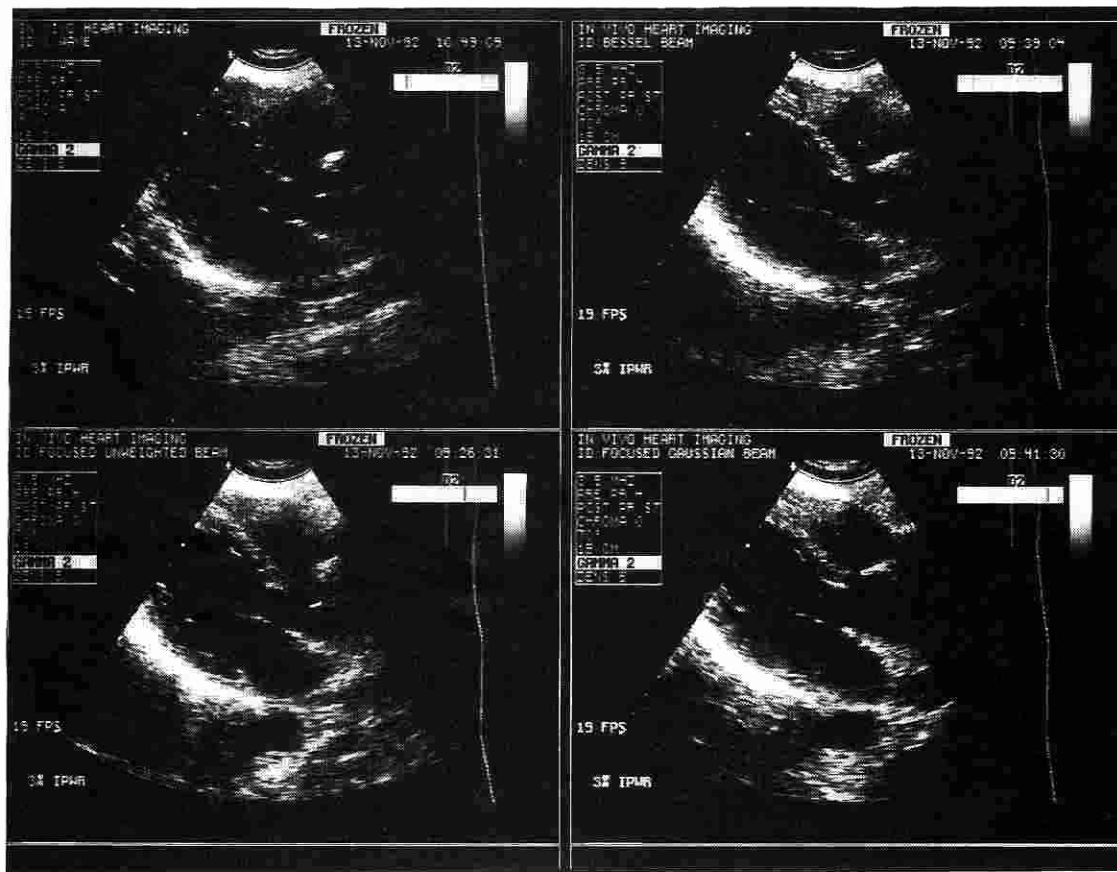
Fig. 9. *In vivo* images (long axis view) of a human heart. The images show approximately the same cross sections and the same moment in a cardiac cycle. This figure has also the same format as that of Fig. 5.

G. Weighted Axicon Beam

To demonstrate the differences between images obtained with the X wave and an Axicon beam [34]–[40], the rear half of the X wave was cut off, resulting in a weighted Axicon beam (the preserved front half of the X wave had a cone shaped wave-front weighted the same as the X wave). Figure 10 shows a comparison of the images obtained with the X wave and the weighted Axicon beam. The images obtained with the X wave were reproduced from Fig. 5 and Fig. 8 (see the X wave panels), respectively. It is seen that the X wave produces images of higher resolution and good contrast over large depth of field while the weighted Axicon beam does not have good resolution and depth of field (see the speckle patterns and the wire targets in Fig. 10). Because the phase of the outer elements are advanced linearly in the weighted Axicon beam, an increase in beam amplitude was experienced (increase with $\sqrt{z}$ for an unweighted Axicon [38]), and the gain of the receiver (TGC) was consequently reduced to obtain images of substantially the same brightness. This helps to reduce the influence of noise on the contrast of the images.

H. Future Work

A new probe with a full 14-element capability will be constructed. Electric noise produced from the digital circuits of the waveform synthesizer will be reduced by stopping the master clock after each transmit process is finished. Power amplifiers of higher voltages will be constructed to increase the penetration depth of the beams. To receive echo signals with better spherical focusing, a full 14-channel dynamic-focusing circuitry can be used. In addition to the transmit calibration, the dynamically focused receiver should also be calibrated to compensate for the variation of sensitivities of the transducer elements and to optimize the delay of each reception channel. In our current prototype system described above, receiver calibration is not possible because a commercial system is used. Imperfections in focusing procedure will have more influence on the limited diffraction beams than on the conventional focused beams since the former rely more on the dynamic focusing to suppress their sidelobes. After the full 14-channel dynamically focused receiver is constructed, reception calibration can be done properly. In addition, the rate at which the focal length is increased should be adjustable to better follow the different average speeds of sound of tissue-mimicking phantoms or patients.

VII. CONCLUSION

The real-time pulse-echo images (*in vitro* and *in vivo*) of a high-quality tissue mimicking phantom and human organs demonstrate that high resolution and good contrast over large depth of field can be obtained with limited diffraction beams. These images are also better than those obtained with a weighted Axicon beam. Conventional focused beams produce similar images only within the focal region. Dynamic-focusing in receive suppresses dramatically the relatively high sidelobes
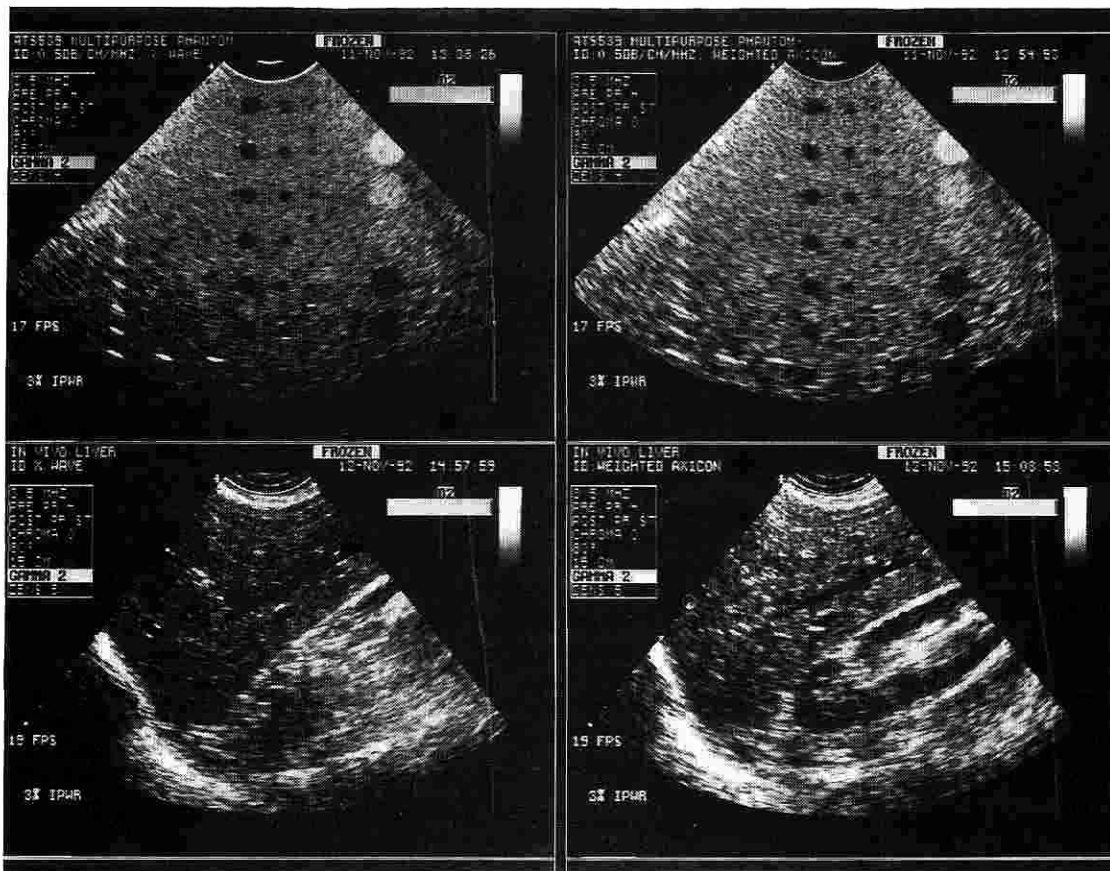
Fig. 10. Comparison of images obtained with X wave and weighted Axicon. The images in the left 2 panels were reproduced from Fig. 5 and Fig. 8 (see X wave panels), respectively. The upper 2 panels show exactly the same cross section of the ATS539 multipurpose phantom and the lower two show approximately the same cross sections of the *in vivo* human liver images.

of the limited diffraction beams. Therefore, the limited diffraction beams have potential usefulness in clinical diagnostic imaging where high resolution with good contrast over a deep depth of field is required without loss in frame rate caused by conventional refocusing methods. Using X waves or other nondispersive limited diffraction beams in both transmit and receive in pulse-echo imaging systems could allow an image restoration technique to be used conveniently and thus produce high resolution and high contrast imaging if the objects studied do not present significant phase aberrations and multiple reflections [33]. Better results could be expected after the above prototype system is technically improved.

ACKNOWLEDGMENT

REFERENCES

[1] J. N. Brittingham, "Focus wave modes in homogeneous Maxwell's equations: transverse electric mode," *J. Appl. Phys.*, vol 54, no. 3, pp. 1179–1189, 1983.

[2] R. W. Ziolkowski, "Exact solutions of the wave equation with complex source locations," *J. Math. Phys.*, vol. 26, no. 4, pp. 861–863, Apr. 1985.

[3] R. W. Ziolkowski, D. K. Lewis, and B. D. Cook, "Evidence of localized wave transmission," *Phys. Rev. Lett.*, vol. 62, no. 2, pp. 147–150, Jan. 1989.

[4] J. Durnin, "Exact solutions for nondiffracting beams—I: The scalar theory," *J. Opt. Soc. Am.*, vol. 4, no. 4, pp. 651–654, 1987.

[5] J. Durnin, J. J. Miceli, Jr., and J. H. Eberly, "Diffraction-free beams," *Phys. Rev. Lett.*, vol. 58, no. 15, pp. 1499–1501, Apr. 1987.

[6] D. K. Hsu, F. J. Margetan, and D. O. Thompson, "Bessel beam ultrasonic transducer: Fabrication method and experimental results," *Appl. Phys. Lett.*, vol. 55, no. 20, pp. 2066–2068, Nov. 1989.

[7] G. Indebetow, "Nondiffracting optical fields: Some remarks on their analysis and synthesis," *J. Opt. Soc. Am. A*, vol. 6, no. 1, pp. 150–152, Jan. 1989.

[8] F. Gori, G. Guattari, and C. Padovani, "Model expansion for J_0-correlated Schell-model sources," *Optics Commun.*, vol. 64, no. 4, pp. 311–316, Nov. 15, 1987.

[9] K. Uehara and H. Kikuchi, "Generation of near diffraction-free laser beams," *Appl. Physics B*, vol. 48, pp. 125–129, 1989.

[10] L. Vicari, "Truncation of nondiffracting beams," *Optics Commun.*, vol. 70, no. 4, pp. 263–266, Mar. 1989.

[11] M. Zahid and M. S. Zubairy, "Directionally of partially coherent Bessel-Gauss beams," *Optics Commun.*, vol. 70, no. 5, pp. 361–364, Apr. 1989.

[12] S. Y. Cai, A. Bhattacharjee, and T. C. Marshall, "'Direction-free' optical beams in inverse free electron laser acceleration," *Nuclear Instruments and Methods in Physics Research, Section A: Accelerators, Spectrometers, Detectors, and Associated Equipment*, vol. 272, no. 1–2, pp. 481–484, Oct. 1988.

[13] J. Lu and J. F. Greenleaf, "Ultrasonic nondiffracting transducer for medical imaging," *IEEE Trans. Ultrason, Ferroelec, Freq. Contr.*, vol. 37, pp. 438–447, Sept., 1990.

[14] J. Lu and J. F. Greenleaf, "Pulse-echo imaging using a nondiffracting beam transducer," *Ultrasound Med. Biol*, vol. 17, no. 3, pp. 265–281, May, 1991.

[15] J. Lu and J. F. Greenleaf, "Evaluation of a nondiffracting transducer for tissue characterization," in *IEEE 1990 Ultrason. Symp. Proc.*, 90CH2938-9, vol. 2, pp. 795–798, 1990.

[16] J. Lu and J. F. Greenleaf, "Diffraction-limited beams and their applications for ultrasonic imaging and tissue characterization," in *New Developments in Ultrasonic Transducers and Transducer Systems*, F. L. Lizzi, ed., Proc. SPIE, vol. 1733, pp. 92–119, 1992.

[17] J. Lu and J. F. Greenleaf, "Formation and propagation of limited diffraction beams," *Acoustic Imaging*, vol. 20, Ben-li Gu, ed. (to be published).

[18] J. Lu and J. F. Greenleaf, "Steering of limited diffraction beams with a two-dimensional array transducer," in *IEEE 1992 Ultrason. Symp. Proc.* 92CH3118-7, vol. 1, pp. 603–607, 1992.

[19] J. Lu and J. F. Greenleaf, "A computational and experimental study of nondiffracting transducer for medical ultrasound," *Ultrasonic Imaging*, vol. 12, no. 2, pp. 146–147, Apr. 1990 (abs.)

[20] J. Lu and J. F. Greenleaf, "Effect on J_0 nondiffracting beam of deleting central elements of J_0 annular array transducer," *Ultrasonic Imaging*, vol. 13, no. 2, p. 203, Apr. 1991 (abs).

[21] J. Lu and J. F. Greenleaf, "Simulation of imaging contrast of nondiffracting beam transducer," *J. Ultrasound Med.* vol. 10, no. 3, (suppl.), p. S4, Mar. 1991 (abs).

[22] J. Lu and J. F. Greenleaf, "Experiment of imaging contrast of J_0 Bessel nondiffracting beam transducer," *J. Ultrasound Med.*, vol. 11, no. 3, (suppl.), p. S43, Mar. 1992 (abs).

[23] J. Lu and J. F. Greenleaf, "Sidelobe reduction of nondiffracting pulse-echo images by deconvolution," *Ultrasonic Imaging*, vol. 14, no. 2, p. 203, Apr. 1992 (abs).

[24] J. Lu and J. F. Greenleaf, "Producing deep depth of field and depth-independent resolution in NDE with limited diffraction beams," *Ultrasonic Imaging*, vol. 15, no. 2, pp. 134–149, Apr. 1993.

[25] J. A. Campbell and S. Soloway, "Generation of a nondiffracting beam with frequency independent beam width," *J. Acoust. Soc. Am.*, vol. 88, no. 5, pp. 2467–2477, Nov. 1990.

[26] J-y. Lu and J. F. Greenleaf, "Nondiffracting X waves—exact solutions to free-space scalar wave equation and their finite aperture realizations," *IEEE Trans. Ultrason., Ferroelec., Freq. Contr*, vol. 39, pp. 19–31, Jan. 1992.

[27] J. Lu and J. F. Greenleaf, "Experimental verification of nondiffracting X waves," *IEEE Trans. Ultrason., Ferroelec., Freq. Contr.*, vol. 39, pp. 441–446, May 1992.

[28] J. Lu and J. F. Greenleaf, "Theory and acoustic experiments of nondiffracting X waves," in *IEEE 1991 Ultrason. Symp. Proc.*, 91CH3079-1, vol. 2, pp. 1155–1159, 1991.

[29] T. K. Song, J. Lu, and J. F. Greenleaf, "Modified X waves with improved field properties," *Ultrasonic Imaging*, vol. 15, no. 1, pp. 36–47, Jan. 1993.

[30] F. John, *Partial Differential Equations*. New York: Springer-Verlag, 1982.

[31] A. V. Oppenheim and R. W. Schafer, *Digital Signal Processing*. Englewood Cliffs, NJ: Prentice-Hall, 1975.

[32] J. W. Goodman, *Introduction to Fourier Optics*. New York: McGraw-Hill, 1968.

[33] M. Fatemi and M. A. Arad, "A novel imaging system based on non-diffracting X waves," in *IEEE 1992 Ultrason. Symp. Proc.* 92CH3118-7, vol. 1, pp. 609–612, 1992.

[34] J. H. Mcleod, "The Axicon: A new type of optical element," *J. Opt. Soc. Am.*, vol. 44, p. 592, 1954.

[35] S. Fujiwara, "Optical properties of conic surfaces. I. Reflecting cone," *J. Opt. Soc. Am.*, vol. 52, pp. 287–292, 1962.

[36] C. B. Burckhardt, H. Hoffmann, and P. A. Grandchamp, "Ultrasound axicon: A device for focusing over a large depth," *J. Acoust. Soc. Am.*, vol. 54, no. 6, pp. 1628–1630, Dec. 1973.

[37] K. Yamada and H. Shimizu, "Conical and toroidal piezoelectric polymer transducers for long range focusing," *IEEE Trans. Sonics Ultrason.*, SU-30, p. 215, 1983.

[38] M. S. Patterson and F. S. Foster, "Acoustic fields of conical radiators," *IEEE Trans. Sonics Ultrason.*, SU-29, no. 2, pp. 83–92, Mar. 1982.

[39] D. R. Dietz, "Apodized conical focusing for ultrasound imaging," *IEEE Trans. Sonics Ultrason.*, SU-29, no. 3, pp. 128–138, May 1982.

[40] M. Moshfeghi, "Sidelobe suppression in annular array and axicon imaging systems," *J. Acoust. Soc. Am.*, vol. 83, no. 6, pp. 2202–2209, June 1988.